

## Magmatic effects of the Cobb hot spot on the Juan de Fuca Ridge

John Chadwick,<sup>1,2</sup> Michael Perfit,<sup>1</sup> Ian Ridley,<sup>3</sup> Ian Jonasson,<sup>4</sup> George Kamenov,<sup>1</sup> William Chadwick,<sup>5</sup> Robert Embley,<sup>5</sup> Petrus le Roux,<sup>6</sup> and Matthew Smith<sup>1</sup>

Received 29 August 2003; revised 23 July 2004; accepted 3 September 2004; published 5 March 2005.

[1] The interaction of the Juan de Fuca Ridge with the Cobb hot spot has had a considerable influence on the magmatism of the Axial Segment of the ridge, the second-order segment that overlies the hot spot. In addition to the construction of the large volcanic edifice of Axial Seamount, the Axial Segment has shallow bathymetry and a prevalence of constructional volcanic features along its 100-km length, suggesting that hot spot–derived magmas supplement and oversupply the ridge. Lavas are generally more primitive at Axial Seamount and more evolved in the Axial Segment rift zones, suggesting that fractional crystallization is enhanced with increasing distance from the hot spot because of a reduced magma supply and more rapid cooling. Although the Cobb hot spot is not an isotopically enriched plume, it produces lavas with some distinct geochemical characteristics relative to normal mid-ocean ridge basalt, such as enrichments in alkalis and highly incompatible trace elements, that can be used as tracers to identify the presence and prevalence of the hot spot influence along the ridge. These characteristics are most prominent at Axial Seamount and decline in gradients along the Axial Segment. The physical model that can best explain the geochemical observations is a scenario in which hot spot and mid-ocean ridge basalt (MORB) magmas mix to varying degrees, with the proportions controlled by the depth to the MORB source. Modeling of two-component mixing suggests that MORB is the dominant component in most Axial Segment basalts.

**Citation:** Chadwick, J., M. Perfit, I. Ridley, I. Jonasson, G. Kamenov, W. Chadwick, R. Embley, P. le Roux, and M. Smith (2005), Magmatic effects of the Cobb hot spot on the Juan de Fuca Ridge, *J. Geophys. Res.*, *110*, B03101, doi:10.1029/2003JB002767.

### 1. Introduction

[2] The central Juan de Fuca Ridge (JdFR) is one of 18 locations on Earth where hot spots and mid-ocean ridge systems interact. As with the other examples, the merging of the JdFR and Cobb hot spot systems has resulted in distinctive bathymetric and morphologic characteristics on the part of the ridge that overlies the hot spot, suggesting a significant magmatic influence on the ridge by the hot spot. In this study, we analyze the spatial geochemical variability (major elements, trace elements, volatiles, and radiogenic isotopes) of basalts from the Axial Segment, the second-order segment that overlies the hot spot, and compare the geochemical attributes of these basalts with those from neighboring segments of the JdFR and the Cobb-Eickelberg seamount chain. These analyses have allowed us to identify

the distinct geochemical characteristics of the Cobb hot spot and to confirm the presence of hot spot magmas on the Axial Segment. They have also provided insight into magma evolution, migration, melting, and mixing processes in this ridge–hot spot system.

#### 1.1. Regional Geology

[3] The Cobb hot spot has produced a chain of seamounts that extends to the NW from the JdFR (Figure 1). The southeastern portion of the chain is collectively referred to as the Cobb-Eickelberg seamounts, but the hot spot track extends discontinuously for a total of nearly 1800 km to the ~33 m.y. Marchand and Chirikof seamounts near the Aleutian Islands of Alaska [Smoot, 1985; Karsten and Delaney, 1989; Desonie and Duncan, 1990; Keller *et al.*, 1997, 2003]. The Cobb chain is flanked by the Pratt-Welker (also known as Kodiak-Bowie) chain to the north and the Pathfinder chain to the south. Axial Seamount, the current location of volcanic activity associated with the hot spot, is located on the axis of the Juan de Fuca Ridge (Figure 1). The January 1998 eruption of Axial Seamount produced extensive lava flows from at least two collinear fissure sources [Embley *et al.*, 1999; Fox *et al.*, 2001; Chadwick *et al.*, 2002]. The geological, hydrothermal, and biological effects of this eruption have been the focus of the National Oceanic and Atmospheric Administration Vents Program's New Millennium Observatory (NeMO) project (available at <http://www.pmel.noaa.gov/vents/nemo/>).

<sup>1</sup>Department of Geological Sciences, University of Florida, Gainesville, Florida, USA.

<sup>2</sup>Now at Department of Geosciences, Idaho State University, Pocatello, Idaho, USA.

<sup>3</sup>U.S. Geological Survey, Denver, Colorado, USA.

<sup>4</sup>Natural Resources Canada, Geological Survey of Canada, Ottawa, Ontario, Canada.

<sup>5</sup>Pacific Marine Environmental Laboratory, NOAA, Hatfield Marine Science Center, Oregon State University, Newport, Oregon, USA.

<sup>6</sup>Department of Terrestrial Magnetism, Carnegie Institution of Washington, Washington, D. C., USA.

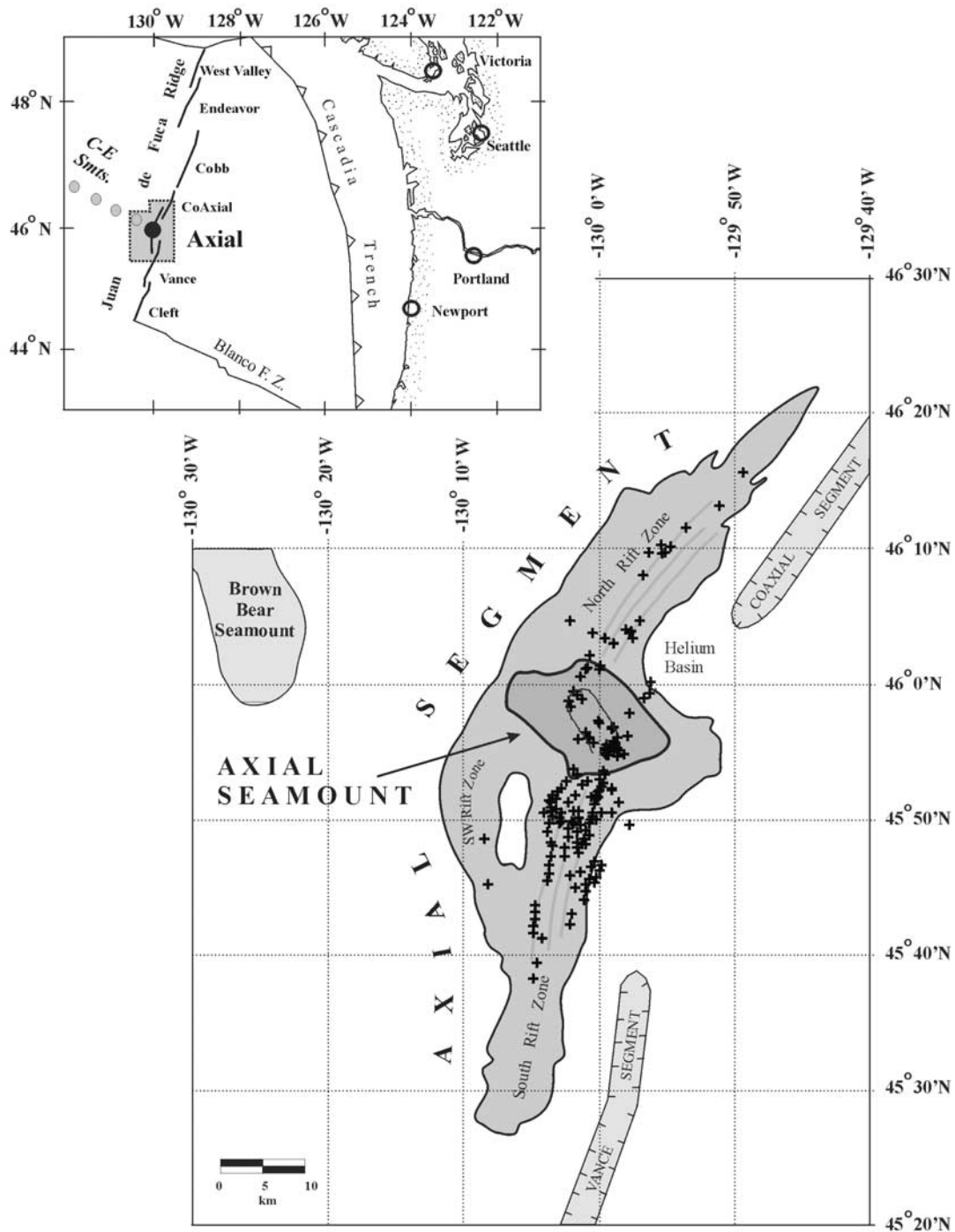


**Figure 1.** The 490-km-long Juan de Fuca Ridge is divided into seven second-order segments (inset). Axial Seamount is the current location of Cobb hot spot volcanism and lies astride the Axial Segment of the Juan de Fuca Ridge. Brown Bear Seamount is the hot spot volcanic center produced prior to Axial Seamount. The edifice of Axial Seamount is demarcated here by the 1650-m isobath contour, where bathymetric contours change from concentric around the seamount to linear and parallel to the trend of the ridge. This contour also separates ridge group and seamount group basalt samples (see text). Locations of the 218 basalt samples retrieved during the National Oceanic and Atmospheric Administration “New Millennium Observatory” cruises and 91 samples collected during earlier expeditions are indicated with pluses.

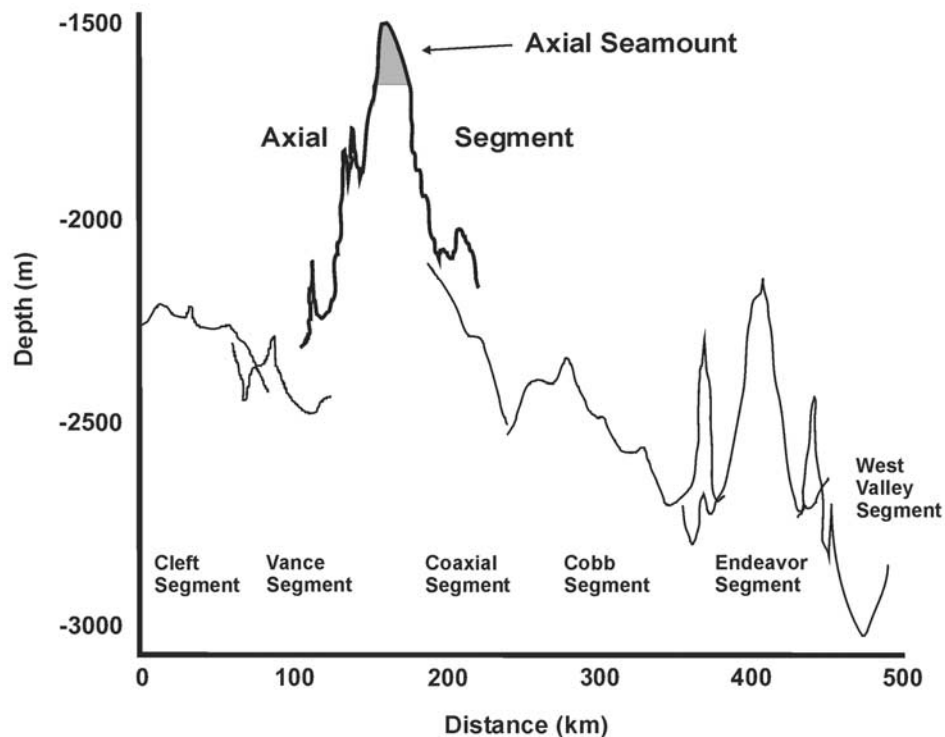


**Figure 2.** Bathymetric profiles along Juan de Fuca Ridge segments are shown. Axial Seamount (shaded area) is the shallowest point on the ridge. Shallow bathymetry on the Axial Segment as a whole suggests that the hot spot's magmatic influence extends beyond Axial Seamount. Vertical exaggeration is  $\sim 250$  times.

[4] The JdFR is the 490-km boundary between the Pacific and Juan de Fuca plates (Figure 1). It is a medium spreading rate system, with a full rate of  $\sim 6$  cm/yr [Vine and Wilson, 1965; Johnson and Embley, 1990]. It is divided into seven second-order ridge segments, including the Axial Segment. The ridge is migrating to the NW at 3.1 cm/yr, movement that brought it into the vicinity of the hot spot  $\sim 0.2$ – $0.7$  m.y. ago [Desonie and Duncan, 1986; Karsten and Delaney, 1989]. A study of the morphological and bathymetric characteristics and the relative age distribution of basalts on the Axial Segment suggest that it has been “captured” by the hot spot, temporarily arresting its migration in a situation similar to the capture of the Mid-Atlantic Ridge by the Iceland hot spot [Oskarsson et al., 1985; Hardarson et al., 1997; Chadwick, 2002].

## 1.2. Characteristics of the Axial Segment

[5] The morphological characteristics of the central part of the JdFR have been described in previous studies on the basis of bathymetry and side-scan sonar imagery [Delaney et al., 1981; Embley et al., 1990; Johnson and Holmes, 1989; Johnson and Embley, 1990]. Axial Seamount is the most prominent bathymetric feature of the ridge, shallowing to  $<1500$  m below sea level at its summit (Figure 2). Side-scan and multibeam sonar surveys have revealed a flat-floored,  $3 \times 8$  km caldera on the summit that opens to the southeast [Embley et al., 1990]. The edifice is connected by a low saddle to the next volcano in the Cobb chain to the northwest, Brown Bear Seamount.

[6] Adjoining Axial Seamount and extending  $\sim 50$  km to the north and south from the caldera are the “rift zones,” prominent ridges offset to the west of the Vance and CoAxial Segment trends (Figure 1). Although the strike of the rift zones is parallel to the rest of the JdFR, there are several important morphological differences between them that can be observed in bathymetric and sonar reflectivity maps. Not including the Axial Seamount edifice, the rift zones themselves are 250–750 m shallower than and nearly twice as wide as the other segments of the JdFR (Figures 1 and 2). In contrast to the other segments that are characterized by axial valleys and a predominance of extensional faults typical of medium spreading rate ridges [Karsten et al., 1986; Johnson and Holmes, 1989; Van Wagoner and Leybourne, 1991; Smith et al., 1994; Embley et al., 2000], the rift zones form a broad, axial rise-like arch dominated by constructional volcanic features [Appelgate, 1990]. A similar change in ridge morphology is observed on the Reykjanes Ridge near the Iceland hot spot [Talwani et al., 1971].

[7] The rift zones have a corrugated appearance, composed of parallel-trending sets of thin (300–500 m wide, up to 150 m high, and up to 15 km long), linear ridges that appear to be dike-fed volcanic constructs. These ridges are larger and more numerous closer to Axial Seamount, and interspersed among them are small (typically  $<1$ -km diameter) cones that are more prevalent with increasing distance from Axial Seamount. Diking of magmas is also suggested by the linear arrangement of eruptive centers for the 1998

eruption of Axial Seamount [Chadwick *et al.*, 2002] and by the locations of earthquake epicenters detected by the Sound Surveillance System hydrophone network during that eruption [Dziak and Fox, 1998, 1999]. These epicenters were observed to migrate progressively southward from the caldera to ~50 km into the south rift zone during the first few days of the 11-day period of activity [Embley *et al.*, 1999].

[8] Despite the dramatic differences from the rest of the ridge the rift zones can be considered an integral part of the JdFR spreading system. They appear to accommodate spreading in the ~60-km gap between the southern end of the CoAxial Segment and the northern end of the Vance Segment, and their curved termini overlap these neighboring segments in the manner of an overlapping spreading center [Embley *et al.*, 2000]. The rift zones and Axial Seamount are collectively referred to as the Axial Segment of the JdFR in this paper.

## 2. Sample Collection and Petrographic Analyses

[9] During the 1998–2001 NeMO cruises a total of 218 rock samples was collected on the Axial Segment (Figure 1). Samples were collected mostly by wax coring on the rift zones, and the Remotely Operated Platform for Ocean Science (ROPOS) submersible was used primarily in the Axial Seamount caldera region, particularly around the 1998 eruption area. The wax core samples were collected up to ~35 km from Axial Seamount to the north and south, and within ~20 km of the caldera they were collected in a high-density pattern (Figure 1), allowing for trends and small-scale differences in geochemistry to be identified. A total of 91 additional samples was collected on previous expeditions to the study area by the *Pisces IV* submersible in 1986, by a grab sampler with integrated video camera (TV-grab) during the 1996 cruise of R/V *Sonne*, and by the *Alvin* submersible and other rock-coring operations between 1988 and 1998. Geochemical analyses of these additional samples supplement this study where noted.

[10] Basalt flow types in the study area include sheet flows, chaotic jumbled flows, pillow basalts, and lobate flows [e.g., Embley *et al.*, 1990]. The freshest samples have thick (1–2 cm) glass rinds that are friable and easily exfoliated, while progressively older samples have thinner rinds and increasing thickness of colloidal Mn oxide coating and associated pelagic sediments. One hand sample, recovered just to the south of the Axial Seamount caldera by ROPOS (R483-6), contains a small gabbroic (olivine-plagioclase-clinopyroxene) xenolith. Most of the basalts are sparsely vesicular (<5% by volume), but six are moderately to highly vesicular (>20%).

[11] Most basalts collected on Axial Seamount are sparsely phyric (<5%), with phenocryst assemblages dominated by plagioclase (An<sub>81</sub> to An<sub>89</sub> measured in six phenocrysts) with rare olivine. A sample from a small cone in the central part of the caldera (*Alvin* sample XL-2087-5) is highly plagioclase phyric (up to 40%) with minor olivine. Most basalts collected from the rift zones are moderately plagioclase phyric (up to 15%).

[12] Plagioclase phenocrysts are typically euhedral to subhedral and <1 mm in diameter, although they commonly form clots of crystals with dimensions up to several milli-

eters. Microphenocrysts and microlites of olivine, plagioclase, clinopyroxene, and opaques commonly occur in the groundmass. The basalts typically have a variolitic texture, with varioles composed of plagioclase and clinopyroxene.

## 3. Geochemical Data

### 3.1. Major Element Geochemistry

[13] Major and minor element compositions of 309 glass samples collected on the Axial Segment are plotted in Figure 3, and representative sample compositions are listed in Table 1.<sup>1</sup> The rocks recovered from the study area are predominantly tholeiitic basalts, with the exception of four basaltic andesites and andesites (SiO<sub>2</sub> up to 58.3 wt %) that were recovered from the eastern side of the north rift zone (RC-49, RC-99, RC-100, and RC-101). These higher-silica rocks are extremely rare along the JdFR, having only been recovered in one other area near the ridge transform intersection at the southern end of the Cleft Segment [Perfit *et al.*, 2001].

[14] Compositional fields for lavas from the Cobb-Eickelberg seamounts and neighboring JdFR segments (Cleft, Vance, CoAxial, and Cobb) are shown in Figure 3 to allow for comparisons and consideration of the geochemical influence of the Cobb hot spot on the composition of Axial Segment lavas. The Endeavour and West Valley segments, north of the Cobb Offset, are not included in the JdFR comparative group because of the enriched mid-ocean ridge basalt (MORB) lavas erupted there [Karsten *et al.*, 1990; Van Wagoner and Leybourne, 1991] and their distance from the study area (>200 km), which precludes them from representing the “local” JdFR MORB for comparison with the Axial Segment.

[15] The basalts in Table 1 have been grouped on the basis of their recovery location, with “seamount group” samples taken from the Axial Seamount caldera and flanks, where bathymetric contours are roughly concentric to the caldera and lavas have flowed downslope from the summit region (Figure 1). “Ridge group” samples are those taken from the rift zones to the north and south of Axial Seamount, where the volcanic morphology and bathymetric contours are clearly dominated by parallel-trending volcanic ridges. This grouping based on morphology suffices to separate lavas that have likely erupted directly from Axial Seamount and those that were erupted from the rift zones, but the grouping does not coincide with any abrupt changes in geochemistry. The boundary between the seamount and ridge groups is roughly demarcated by the 1650-m isobath contour that surrounds Axial Seamount.

[16] Axial Segment basalts have major element compositions that are largely similar to JdFR MORB, but most have notable alkali enrichments relative to the JdFR lavas at comparable MgO values (Figure 3). Alkali enrichment was noted in previous studies as a prominent geochemical expression of the Cobb hot spot [Desonie and Duncan, 1990; Rhodes *et al.*, 1990].

[17] Basalts from the Seamount and Ridge groups have similar major element compositional ranges, but the sea-

<sup>1</sup>Auxiliary material is available at <ftp://ftp.agu.org/apend/jb/2003JB002767>.

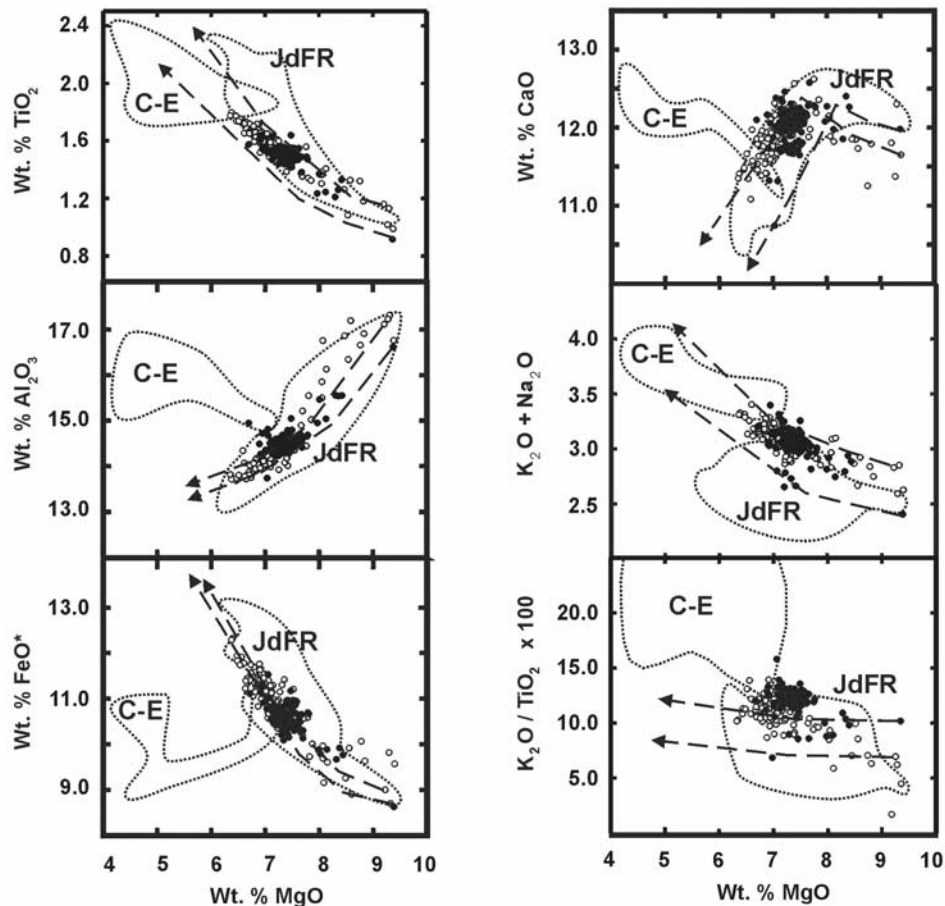


**Figure 3.** Major element oxide variation for 309 basalt samples is shown, divided into the seamount group (solid circles) and ridge group (open circles). Comparisons with the Juan de Fuca Ridge (JdFR) and Cobb hot spot (Cobb-Eickelberg (C-E) seamounts) fields show that the Axial Segment samples have geochemical characteristics that are generally more comparable to the JdFR than the hot spot lavas, although alkali concentrations are intermediate between the two. Low-pressure (1 kbar), hydrous (0.2% H<sub>2</sub>O) liquid lines of descent are shown for two mafic basalts (dashed lines). On the basis of replicate analyses of standards over the period of time the analyses were done, error bars (standard deviations) of the elemental concentrations for the major element oxides shown are approximately the size of the symbols. Major and trace element data used for comparative purposes in this paper are from the following sources: Cobb-Eickelberg seamounts data are from *Desonie and Duncan* [1990] and *Liias* [1986], and JdFR data are from *Eaby et al.* [1984], *Smith et al.* [1994], and this study for the Cleft Segment; *Eaby et al.* [1984], M. Perfit (unpublished data, 1998), and this study for the Vance Segment; *Eaby et al.* [1984] and *Smith* [1999] for the CoAxial Segment; and *Eaby et al.* [1984] and *Van Wagoner and Leybourne* [1991] for the Cobb Segment.

mount group basalts are much more homogenous, with the vast majority (161 of 169) falling in a comparatively small range between 6.9 and 7.8 wt % MgO. The low major element variability of the seamount group may be due in part to a sampling bias, as many of the basalts from Axial Seamount were collected by submersibles in confined sampling areas, and numerous samples may come from single flows. However, when this bias is removed and only samples from diverse parts of the caldera and flanks are examined, a high degree of homogeneity is still demonstrable [Perfit *et al.*, 1988]. Basalts from the ridge group are generally more evolved and have significantly more compositional variability. This variability is largely due to spatial gradients in major element concentrations, with

compatible major elements decreasing and incompatible major elements increasing with increasing distance from the seamount (Figure 4).

[18] Scattered along the Axial Segment are about a dozen more primitive basalts that clearly do not conform to the regional geochemical gradients (Figure 4). Many of these were collected from small volcanic cones in the rift zones, but others were collected from parts of the rift zones with no anomalous bathymetric features and from the flanks and caldera of Axial Seamount.

[19] Low-pressure liquid lines of descent (LLD) calculations [Danyushevsky, 2001] were used to model the low-pressure fractional crystallization behavior of the Axial Segment magmas (Figure 3). LLD models were run at 1 kbar,

**Table 1.** Major Element Oxide Chemistry of Representative Seamount Group and Ridge Group Samples<sup>a</sup>

Sample	Longitude	Latitude	SiO <sub>2</sub>	Al <sub>2</sub> O <sub>3</sub>	TiO <sub>2</sub>	FeO*	MnO	MgO	CaO	K <sub>2</sub> O	Na <sub>2</sub> O	P <sub>2</sub> O <sub>5</sub>	Total
<i>Seamount Group</i>													
R461-25	-129.979	45.927	50.08	14.94	1.23	9.87	0.20	7.96	12.07	0.12	2.69	0.10	99.27
R462-15	-129.981	45.933	50.02	14.45	1.55	10.71	0.21	7.34	12.02	0.19	2.96	0.14	99.59
R479-15	-130.014	45.933	49.95	14.61	1.53	10.62	0.22	7.30	12.10	0.19	2.95	0.15	99.63
R483-06	-129.982	45.933	49.51	14.21	1.50	10.71	0.20	7.20	12.10	0.18	2.86	0.14	98.62
R488-16	-129.981	45.933	49.46	14.23	1.51	10.67	0.19	7.17	12.01	0.18	2.90	0.15	98.47
R491-22	-129.981	45.934	50.01	14.63	1.48	10.28	0.19	7.62	12.17	0.18	2.85	0.13	99.55
R497-20	-130.016	46.018	49.96	14.51	1.46	10.48	0.20	7.13	11.94	0.20	3.06	0.16	99.10
R501-02	-129.992	45.920	49.73	14.59	1.51	10.36	0.19	7.39	12.19	0.19	2.92	0.16	99.24
R501-04	-129.989	45.920	49.80	14.37	1.49	10.54	0.20	7.32	12.10	0.18	2.92	0.15	99.06
R501-06	-129.986	45.920	49.88	14.44	1.50	10.51	0.19	7.31	11.89	0.18	2.92	0.16	98.97
R501-07	-129.981	45.920	49.71	14.36	1.49	10.50	0.19	7.32	12.17	0.18	2.91	0.16	99.00
R501-10	-129.982	45.924	49.83	14.33	1.51	10.62	0.20	7.21	12.07	0.18	2.60	0.15	98.70
R501-12	-129.987	45.924	49.54	14.47	1.48	10.22	0.20	7.40	12.22	0.18	2.48	0.14	98.33
<i>Ridge Group</i>													
98-RC-11	-130.006	45.850	50.08	14.33	1.52	10.62	0.20	7.16	11.85	0.20	2.94	0.13	99.03
99-RC-55	-130.072	45.687	50.01	14.05	1.69	11.36	0.22	6.78	11.85	0.18	2.91	0.13	99.18
99-RC-64	-130.080	45.727	49.99	13.77	1.71	11.39	0.23	6.62	11.57	0.21	2.97	0.19	98.66
99-RC-70	-130.019	45.734	49.97	14.36	1.45	10.46	0.21	7.21	12.21	0.13	2.80	0.14	98.94
99-RC-75	-130.012	45.774	49.89	14.06	1.64	11.22	0.22	6.61	11.97	0.18	2.94	0.15	98.89
99-RC-85	-130.060	45.853	50.00	13.98	1.55	10.81	0.20	7.09	12.02	0.17	2.85	0.15	98.81
99-RC-88	-130.039	45.811	49.93	13.95	1.59	11.03	0.20	6.97	11.85	0.17	2.95	0.16	98.79
99-RC-89	-130.024	45.825	50.10	13.88	1.64	11.06	0.20	6.75	11.77	0.20	3.01	0.18	98.80
99-RC-91	-130.028	45.805	49.73	14.00	1.54	10.68	0.21	7.41	12.07	0.14	3.00	0.14	98.92
99-RC-102	-130.037	46.077	49.65	14.10	1.52	10.62	0.21	7.08	11.97	0.15	2.88	0.13	98.30
99-RC-108	-130.064	45.817	49.95	13.94	1.65	11.19	0.22	6.82	11.62	0.19	3.04	0.13	98.73
R465-01	-129.986	45.869	50.12	14.20	1.53	10.94	0.19	7.04	11.74	0.20	2.98	0.14	99.08
R494-04	-130.004	45.862	50.12	14.43	1.56	10.84	0.20	7.11	11.80	0.18	2.90	0.15	99.27

<sup>a</sup>All analyses are performed on natural glasses by electron microprobe. Sample numbers refer to *ROPOS* dive numbers (R-) or New Millennium Observatory wax cores (98-RC-). FeO\* is all Fe calculated as FeO. *ROPOS* sample locations were derived from acoustic navigation fixes calibrated with GPS; wax core sample locations are the GPS position of the ship. Major element data are available as auxiliary material. Analytical methods are discussed in Appendix A.

an appropriate pressure considering the large magma storage body identified at 2.25–3.5 km depth under Axial Seamount with seismic tomographic techniques [West *et al.*, 2001], and with 0.2% H<sub>2</sub>O, the average water content of eight Axial Segment basalts measured in this study. Using some of the most mafic basalts as parents, the LLD suggest that major element variability is due in large part to fractional crystallization, but the wide scatter of the data is evidence that they have originated and evolved from a range of parental magmas [Lüas, 1986; Rhodes *et al.*, 1990].

### 3.2. Isotope Geochemistry

[20] Radiogenic isotope ratios (<sup>87</sup>Sr/<sup>86</sup>Sr, <sup>143</sup>Nd/<sup>144</sup>Nd, <sup>206</sup>Pb/<sup>204</sup>Pb, <sup>207</sup>Pb/<sup>204</sup>Pb, and <sup>208</sup>Pb/<sup>204</sup>Pb) for Axial Segment basalts are listed in Table 2 and plotted in Figure 5. Radiogenic isotopes are usually effective tools for identifying cogenetic groups of rocks because the ratios are not changed by melting or fractional crystallization. However, basalts from the Cobb-Eickelberg hot spot chain and Axial Segment have normal mid-oceanic ridge basalt (NMORB)-like Sr and Nd isotopic compositions [Eaby *et al.*, 1984; Lüas, 1986; Hegner and Tatsumoto, 1987; Desonie and Duncan, 1990; Rhodes *et al.*, 1990] that are virtually indistinguishable from most of the neighboring JdFR segments (with the exception of CoAxial Segment basalts that have the lowest <sup>87</sup>Sr/<sup>86</sup>Sr on the JdFR) and regional eastern Pacific MORB (JdFR, Gorda and Explorer Ridges, and East Pacific Rise), rendering them ineffective for the purpose of identifying different sources (i.e., hot spot versus ridge) in this case.

[21] Hegner and Tatsumoto [1987] noted that Cobb-Eickelberg seamount basalts may have Pb isotopic compositions that are slightly enriched relative to MORB, and this enrichment is particularly apparent in <sup>206</sup>Pb/<sup>204</sup>Pb values (Figure 5). Axial Segment basalt compositions largely overlap with Cobb hot spot and regional eastern Pacific MORB variability, but some appear to be enriched relative to the neighboring segments of the JdFR. However, there are currently a limited number of Pb isotope measurements available for the JdFR, which likely leads to an inaccurate perception of the true compositional variability of the ridge. This limitation precludes a definitive comparison between the ridge, hot spot, and Axial Segment.

### 3.3. Trace Element Geochemistry

[22] Trace element and H<sub>2</sub>O concentrations and elemental ratios in Axial Segment basalts are shown in Figure 6, and the compositions of representative samples are presented in Table 3, where they are divided into seamount and ridge groups in the same fashion as the major elements. There is a clear distinction in the concentrations and ratios of most trace elements between Cobb hot spot and JdFR basalts. Axial Segment basalts have compositional ranges that are generally intermediate between the two but overlap with the more depleted JdFR compositional variability. Volatile and halogen concentrations for selected Axial Segment basalts are presented in Table 4, and these values largely fall within JdFR ranges, although H<sub>2</sub>O values are as high as the most water-rich JdFR samples (Figure 6).

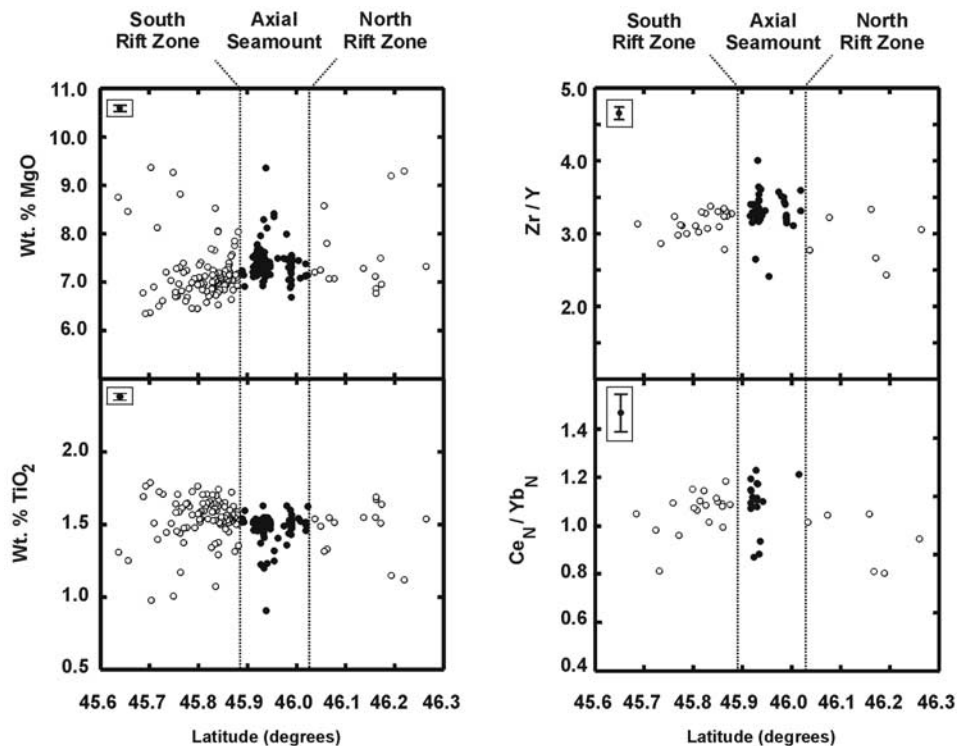


**Figure 4.** Major and trace element concentrations along the Axial Segment have highest or lowest values in the seamount group (solid circles) and exhibit gradients that decline or increase in the ridge group (open circles). Decreasing gradients in compatible major elements (e.g., MgO) and correlative increases in incompatible major elements (e.g., TiO<sub>2</sub>) with distance from Axial Seamount are observed. Incompatible trace element concentrations and ratios show decreasing gradients with distance from the hot spot. A few basalts with more primitive major element compositions (e.g., >7.8% MgO and <1.3% TiO<sub>2</sub>) and more depleted trace element compositions (e.g., Zr/Y < 2.7 and Ce/Yb < 0.9) do not fall along the observed trends.

[23] As with the compatible major elements, incompatible trace element concentrations peak at Axial Seamount and decrease in gradients with increasing distance from the seamount along the ridge (Figure 4). For example, Nb, Sr, and Zr concentrations in the seamount group range in excess of 7, 159, and 120 ppm, respectively, but in the distal south rift zone, concentrations fall to <5, <145, and <100 ppm in samples with lower MgO contents. Similar gradients have been identified along mid-ocean ridges at other ridge-hot spot interactions (Iceland, Azores, and Galapagos), albeit over longer distances [e.g., Hart *et al.*, 1973, 1992; Schilling, 1973; Schilling *et al.*, 1976; Elliot *et al.*, 1991; Murton *et al.*, 2002; Schilling *et al.*, 2003].

[24] As with the major elements, there are a few basalts with disparate trace element compositions that do not adhere to the general geochemical trends and compositional groupings (Figures 4, 6, and 7). These basalts have depleted compositions that are similar to NMORB from neighboring JdFR segments (e.g., Ce<sub>N</sub>/Yb<sub>N</sub> < 0.9 and Zr/Y < 2.7). Many of these depleted basalts also have the more primitive major element compositions reported in section 3.1. They also have distinct rare earth element (REE) patterns (e.g., Ce<sub>N</sub>/Yb<sub>N</sub> for samples R461-25 = 0.87 and RC-70 = 0.82) that mimic NMORB from the JdFR (Figure 7), whereas most basalts from the Axial Segment have relatively flat REE patterns (Ce<sub>N</sub>/Yb<sub>N</sub> ~ 0.95–1.2). Mantle-normalized dia-

grams (Figure 7) show similar results, with most Axial Segment basalts exhibiting trends that are intermediate between enriched Cobb-Eickelberg seamounts and depleted JdFR trends and a few depleted samples that resemble JdFR MORB patterns.

#### 4. Discussion

[25] The large number of samples analyzed in this study collected from a substantial portion of the Axial

**Table 2.** Isotopic Compositions of Representative Axial Segment Basalts<sup>a</sup>

Sample	<sup>87</sup> Sr/ <sup>86</sup> Sr	<sup>143</sup> Nd/ <sup>144</sup> Nd	<sup>206</sup> Pb/ <sup>204</sup> Pb	<sup>207</sup> Pb/ <sup>204</sup> Pb	<sup>208</sup> Pb/ <sup>204</sup> Pb
R461-25	0.702436	0.513155	18.382	15.567	38.004
R491-22	0.702458	0.513117	18.323	15.564	37.959
R494-5	0.702519	0.513145	8.490	15.523	38.012
R501-2	0.702539	0.513111	18.529	15.498	37.997
R501-7	0.702522	0.513131	18.341	15.567	37.978
99-RC-108	0.702548	0.513103	18.638	15.543	38.310
98-RC-70			18.455	15.546	38.061
99-RC-85			18.526	15.529	38.087
99-RC-88			18.542	15.535	38.087
99-RC-91			18.418	15.559	38.051

<sup>a</sup>Sr isotopes were acquired using thermal ionization mass spectrometer; Nd and Pb were acquired using inductively coupled plasma mass spectrometry (see Appendix A for methods).

Segment has allowed for a detailed examination of the spatial variability of lava compositions along the segment, providing insight into magmatic processes resulting from the interaction of the ridge and hot spot systems. On the largest scale the lack of a strong geochemical contrast between seamount group and ridge group basalts and the gradients in major and trace element concentrations along the ridge indicate that lavas from the two groups are genetically related and that the hot spot influence extends beyond the construction of the Axial Seamount edifice to the rest of the Axial Segment. This observation supports the evidence from the shallow bathymetry (Figure 2) and abundance of volcanic features on the Axial Segment that

suggests that hot spot magmas locally supplement and “oversupply” the ridge.

[26] The restricted compositional variation of seamount group basalts possibly reflects long-term storage and homogenization of magmas in the large chamber or lens identified beneath Axial Seamount [Perfit *et al.*, 1988; Rhodes, 1988; West *et al.*, 2001; G. Kent, personal communication, 2004]. The geochemical similarities between seamount and proximal ridge group basalts (Figure 4) also suggest that some of the lavas erupted in the rift zones may have been laterally transported from Axial Seamount into the rift zones via dikes. The linear volcanic ridge morphology of the rift zones, the linear arrangement of the 1998 eruptive vents, and the 50-km migration of earthquakes along the south rift zone during the eruption [Dziak and Fox, 1998, 1999] support such a model of lateral melt transport.

#### 4.1. Fractional Crystallization Effects

[27] The gradients in major element concentrations along the Axial Segment, with generally more primitive basalts erupted on and near Axial Seamount and progressively more evolved basalts erupted with increasing distance from the seamount along the rift zones, suggest an increasing efficiency of fractional crystallization with distance from the hot spot (Figure 4). This is possibly a consequence of the reduction in magma supply along the rift zones and resultant more rapid cooling [e.g., Christie and Sinton, 1981] or a phenomenon equivalent to the “cold edge effect” [Langmuir and Bender, 1984], which is commonly observed near ridge transform intersections or at the end of overlapping ridge segments. Basalts erupted on and near Axial Seamount are likely erupted directly from a large magma chamber [West *et al.*, 2001] in a comparatively hotter environment, resulting in more limited cooling and fractional crystallization of the magmas. Farther along the rift zones to the north and south, a decrease in magma supply may lead to smaller, ephemeral magma bodies and cooler crust, resulting in enhanced crystal fractionation and evolved lavas. Recent multichannel seismic data support this hypothesis, revealing significant melt regions beneath Axial Seamount but none under the rift zones (G. Kent, personal communication,

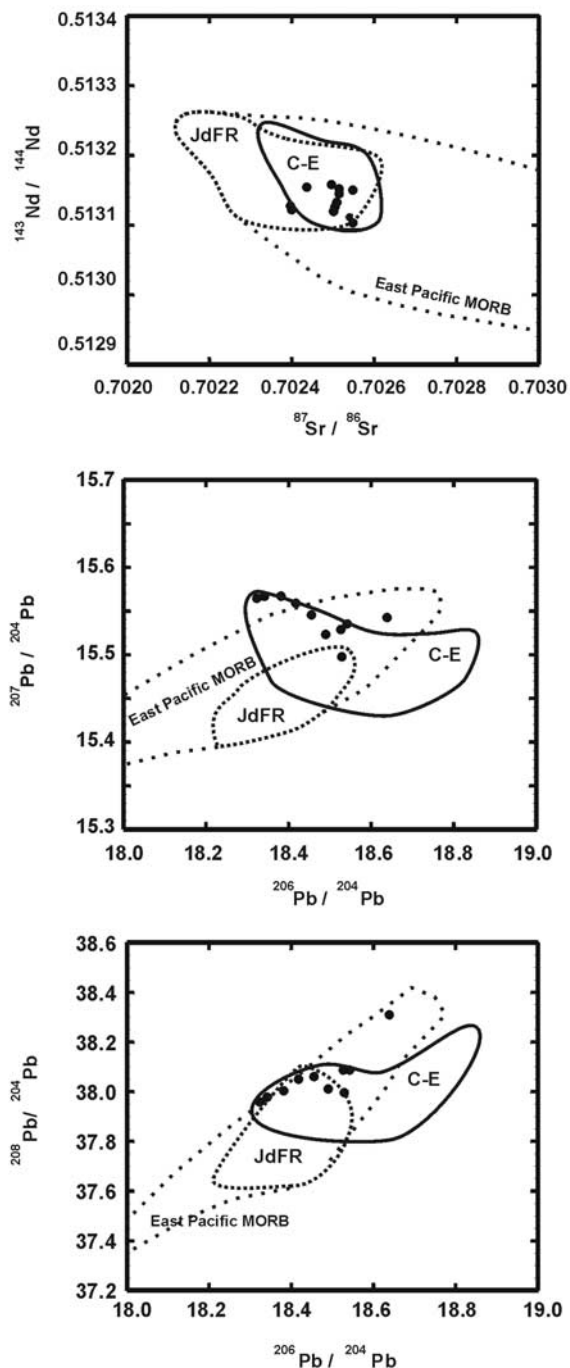


**Figure 5.** C-E basalts and east Pacific (JdFR, Gorda Ridge, Explorer Ridge, and East Pacific Rise) mid-ocean ridge basalt (MORB) have overlapping Sr and Nd isotopic compositions, prohibiting the use of these isotopes for identification of distinct mantle sources in this study. Cobb hot spot and Axial Segment (solid dots) basalts appear to be enriched relative to JdFR in their Pb isotopic compositions, although the true isotopic variability of the JdFR is not clear because of limited available Pb isotopic data. C-E isotopic data are from Hegner and Tatsumoto [1989], Desonie and Duncan [1990], and this study; JdFR data are from Church and Tatsumoto [1975], Hegner and Tatsumoto [1987], M. Smith (unpublished data, 1998), and this study; eastern Pacific MORB data are from Petrological Database of the Ocean Floor (see <http://petdb.ldeo.columbia.edu/petdb/enterdatabase.htm>).

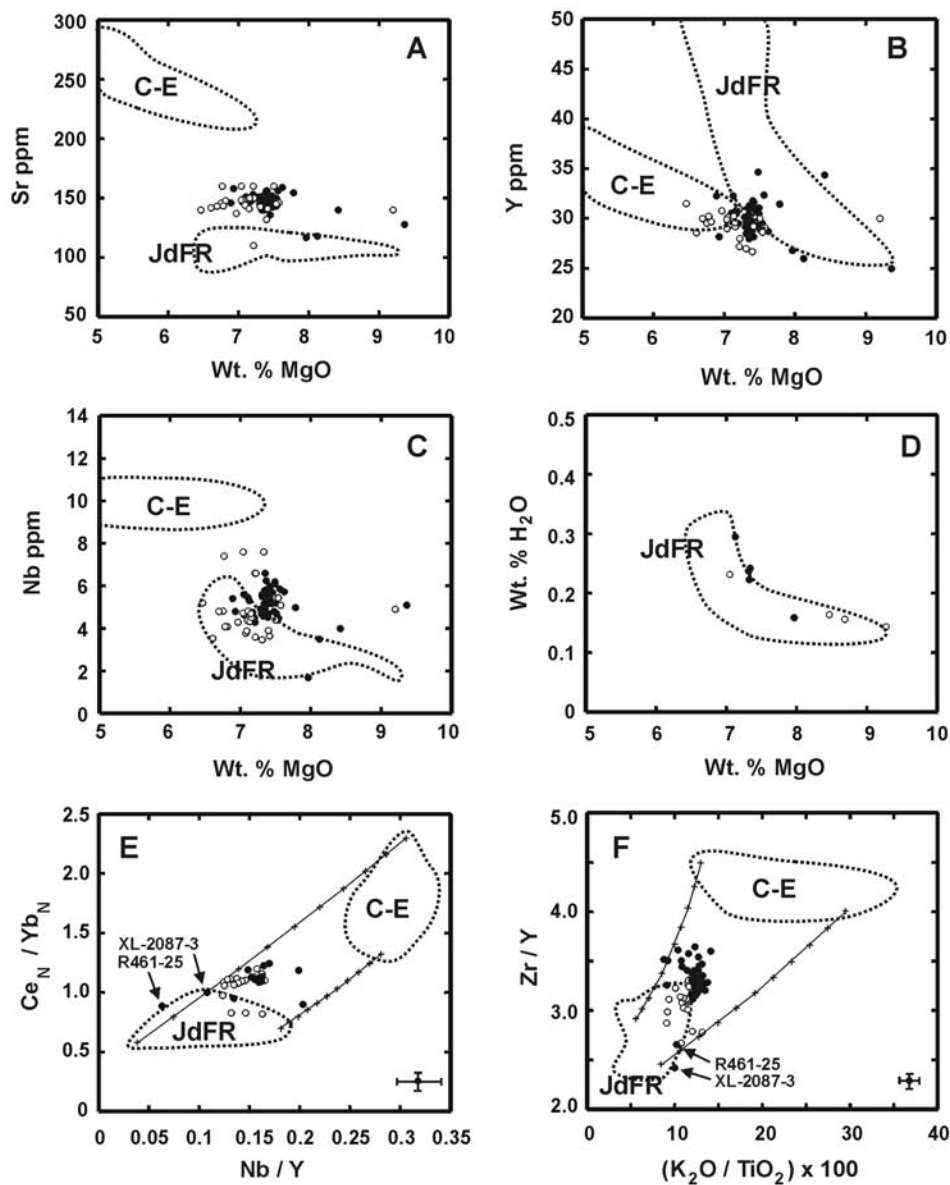


**Figure 6.** (a–f) Axial Segment basalts have incompatible and compatible trace element compositions and ratios that are intermediate between the JdFR and C-E fields. As shown in Figure 4, average values of seamount group (solid dots) incompatible element concentrations and elemental ratios are higher than averages for the ridge group (open circles). However, a few seamount group samples, such as R461-25 and XL-2087-3 (arrows), have more depleted, MORB-like compositions. Mixing lines (indicated in Figures 6e and 6f) show that JdFR and C-E magmas are viable mixing end-members for Axial Segment basalts. Tick marks on mixing lines correspond to 10% mixing increments between C-E and JdFR end-members. No volatile data are available for the C-E Seamounts.

2004). The progressive increase in the depth of the ridge from near Axial Seamount to the distal ends of the segment (Figure 2) is also evidence for a diminished supply of magma to the segment's ends, and the resulting thinner crust would enhance cooling.

[28] Fractional crystallization has resulted in progressive depletions in compatible major elements and progressive enrichments in incompatible major elements with increasing distance from Axial Seamount (Figure 4). Sr appears to behave compatibly, exhibiting a decreasing trend in its concentration with distance from Axial Seamount that is

similar to the compatible major elements. However, incompatible trace element concentrations (including  $K_2O$ ) also exhibit progressive depletions with decreasing MgO and increasing distance from the hot spot, resulting in basalts that are generally more evolved and yet more incompatible element depleted toward the distal ends of the segment (Figure 4). These relationships indicate that variable fractional crystallization cannot be the sole process controlling the geochemical variability of Axial Segment basalts and is clearly not the most important process controlling trace element variability, and the

**Table 3.** Trace Element Chemistry of Representative Seamount Group and Ridge Group Samples<sup>a</sup>

Seamount Group Samples												
	R461-25 <sup>b</sup>	R462-15	R479-15	R483-06	R488-16	R491-22	R497-20	R501-02	R501-07	R501-10	R501-12	
<i>XRF, ppm</i>												
Zr	71.1	98.4	93.3	97.6	98.7	95.7	116.3	96.5	98.6	101.3	95.4	
Sr	116.8	148.5	145.4	148.9	149.4	159.1	148.5	154.3	149.5	153.2	154.3	
Y	26.8	31.1	29.2	29.5	29.3	28.7	32.3	28.4	30.1	30.9	28.6	
Nb	1.7	4.6	4.7	4.5	4.8	5.7	5.3	4.5	4.7	4.3	4.7	
Sc	55.2	59.5	58.9	na	64.2	60.8	56.2	55.5	61.2	66.3	61.6	
Rb	1.1	2.1	1.3	2.2	2.7	2.5	2.8	2.9	1.9	2.5	1.9	
<i>Selected Trace Elements, ppm, ICP-MS</i>												
Cr	317	279	295	275	282	302	276	295	283	199	298	
V	263	295	290	291	297	281	287	284	296	293	283	
Ni	61	46	47	44	44	55	44	51	46	44	52	
Ta	0.17	0.3	0.32	0.34	0.33	0.33	0.35	0.31	0.34	0.32	0.31	
U	0.07	0.11	0.14	0.28	0.15	0.12	0.18	0.13	0.12	0.11	0.11	
<i>Rare Earth Elements, ppm, ICP-MS</i>												
La	2.8	4.7	4.9	4.9	4.8	5.1	5.5	4.7	4.8	4.9	4.8	
Ce	8.7	13.6	13.5	13.2	13.1	13.6	15.2	13.0	13.4	13.6	13.3	
Pr	1.5	2.1	2.2	2.1	2.1	2.2	2.3	2.1	2.1	2.1	2.2	
Nd	8.2	10.9	11.7	11.2	11.4	11.2	11.9	10.9	11.1	11.3	10.9	
Sm	2.7	3.5	3.5	3.4	3.8	3.5	3.8	3.7	3.6	3.8	3.6	
Eu	1.0	1.3	1.4	1.4	1.4	1.4	1.4	1.4	1.4	1.4	1.3	
Gd	3.9	4.7	4.8	4.8	4.9	4.7	5.1	4.8	4.7	4.8	4.6	
Tb	0.7	0.8	0.8	0.9	0.9	0.8	0.9	0.8	0.9	0.9	0.8	
Dy	4.7	5.2	5.3	5.1	5.5	5.2	5.4	5.3	5.4	5.4	5.3	
Ho	1.0	1.1	1.2	1.1	1.2	1.1	1.2	1.2	1.2	1.2	1.2	
Er	2.7	2.9	3.1	3.0	3.1	2.9	3.2	3.1	3.1	3.2	3.1	
Tm	0.4	0.5	0.4	0.5	0.5	0.5	0.5	0.5	0.5	0.5	0.5	
Yb	2.6	3.0	3.2	3.1	3.2	3.0	3.2	3.2	3.2	3.3	3.1	
Lu	0.4	0.5	0.5	0.5	0.5	0.5	0.5	0.5	0.5	0.5	0.5	
Ridge Group Samples												
	98-RC-11	99-RC-102	99-RC-108	99-RC-55	99-RC-70 <sup>c</sup>	99-RC-75	99-RC-85	99-RC-88	99-RC-89	99-RC-91	R465-01	R494-04
<i>XRF, ppm</i>												
Zr	96.6	97.1	98.0	94.9	78.0	89.2	91.2	93.1	96.9	90.9	97.5	98.3
Sr	149.9	146.7	147.9	143.5	110.2	141.8	144.0	137.1	145.7	141.0	148.5	148.9
Y	29.2	30.1	29.7	30.3	27.2	28.6	29.5	30.8	29.6	29.2	29.9	29.4
Nb	4.5	3.8	4.1	4.1	3.6	3.5	3.9	4.3	4.8	3.6	4.7	4.8
Sc	58.8	63.9	53.1	64.5	na	57.8	46.9	57.6	58.7	55.0	60.1	61.6
Rb	2.2	1.4	1.6	1.9	1.4	2.0	2.8	2.7	2.3	1.5	1.5	2.4
<i>Selected Trace Elements, ppm, ICP-MS</i>												
Cr	309	315	331	308	309	282	300	262	287	330	285	280
V	291	289	295	286	255	276	278	289	296	273	290	294
Ni	53	52	42	55	53	48	51	48	44	53	47	44
Ta	0.31	0.27	0.3	0.26	0.20	0.27	0.28	0.3	0.32	0.24	0.31	0.32
U	0.11	0.1	0.11	0.09	0.08	0.1	0.1	0.1	0.13	0.09	0.12	0.11
<i>Rare Earth Elements, ppm, ICP-MS</i>												
La	4.8	4.3	4.8	4.4	3.1	4.4	4.3	4.3	5.1	3.9	4.6	4.9
Ce	12.9	12.7	13.2	12.4	9.0	11.9	12.4	12.6	13.7	12.0	13.1	13.4
Pr	2.1	1.9	2.1	2.0	1.5	2.0	1.9	1.9	2.2	1.9	2.1	2.2
Nd	10.9	10.8	11.3	10.8	7.9	10.3	10.1	10.5	11.3	10.2	10.7	11.5
Sm	3.4	3.5	3.4	3.4	3.0	3.2	3.4	3.5	3.5	3.3	3.3	3.7
Eu	1.3	1.3	1.3	1.3	1.2	1.3	1.3	1.3	1.3	1.2	1.4	1.4
Gd	4.8	4.8	4.7	4.7	4.1	4.5	4.5	4.9	4.9	4.5	4.6	4.8
Tb	0.8	0.9	0.8	0.8	0.8	0.8	0.8	0.8	0.8	0.8	0.8	0.9
Dy	5.1	5.3	5.3	5.2	4.9	5.1	4.9	5.2	5.4	5.0	5.2	5.4
Ho	1.1	1.2	1.2	1.1	1.1	1.1	1.1	1.1	1.2	1.1	1.1	1.2
Er	3.0	3.2	3.1	3.0	2.9	3.0	2.9	3.1	3.2	2.9	2.9	3.1
Tm	0.5	0.5	0.5	0.5	0.4	0.5	0.4	0.5	0.5	0.5	0.5	0.5
Yb	3.0	3.2	3.1	3.1	2.9	3.2	2.9	3.1	3.1	2.9	2.9	3.2
Lu	0.5	0.5	0.5	0.5	0.5	0.5	0.5	0.5	0.5	0.5	0.5	0.5

<sup>a</sup>XRF and inductively coupled plasma–mass spectrometry (ICP-MS) analyses are performed on crystal-free glass powders; na means not analyzed.

<sup>b</sup>R461-25 represents the atypical, more depleted group of basalts (see text).

<sup>c</sup>RC-70 represents the atypical, more depleted group of basalts (see text).

**Table 4.** Volatile and Halogen Compositions of Selected Basalts<sup>a</sup>

Sample	H <sub>2</sub> O, wt %	CO <sub>2</sub> , ppm	F, ppm	S, ppm	Cl, ppm
98-RC-46	0.14	201	122	965	15
99-RC-54	0.16	116	167	1010	78
R461-16	0.22	334	224	1321	135
R461-25	0.16	126	175	1331	62
R462-15	0.24	218	240	1456	189
R465-2	0.23	107	244	1470	164
R497-20	0.30	178	239	1256	381
R501-6	0.24	237	234	1447	151

<sup>a</sup>Analyses are performed on glass chips using the 6f ion probe at the Carnegie Institute of Washington (see Appendix A for methods).

relationships demonstrate that melting and/or mixing effects are also required.

#### 4.2. Melting Scenarios

[29] If the effects of melting are the primary process controlling trace element variation on the Axial Segment and all of its lavas are derived from a single source (e.g., hot spot or MORB with no mixing), a lower melt fraction could be invoked to produce the more enriched lavas and higher Na<sub>8.0</sub> values observed in the seamount group relative to the ridge group [after *Klein and Langmuir, 1987*]. A significantly deeper melt column would be required to explain the much higher magmatic volumes produced by Axial Seamount if this is the case. However, lower Fe<sub>8.0</sub> values measured in the seamount group are indicative of shallower melting, and this observation suggests an unlikely situation

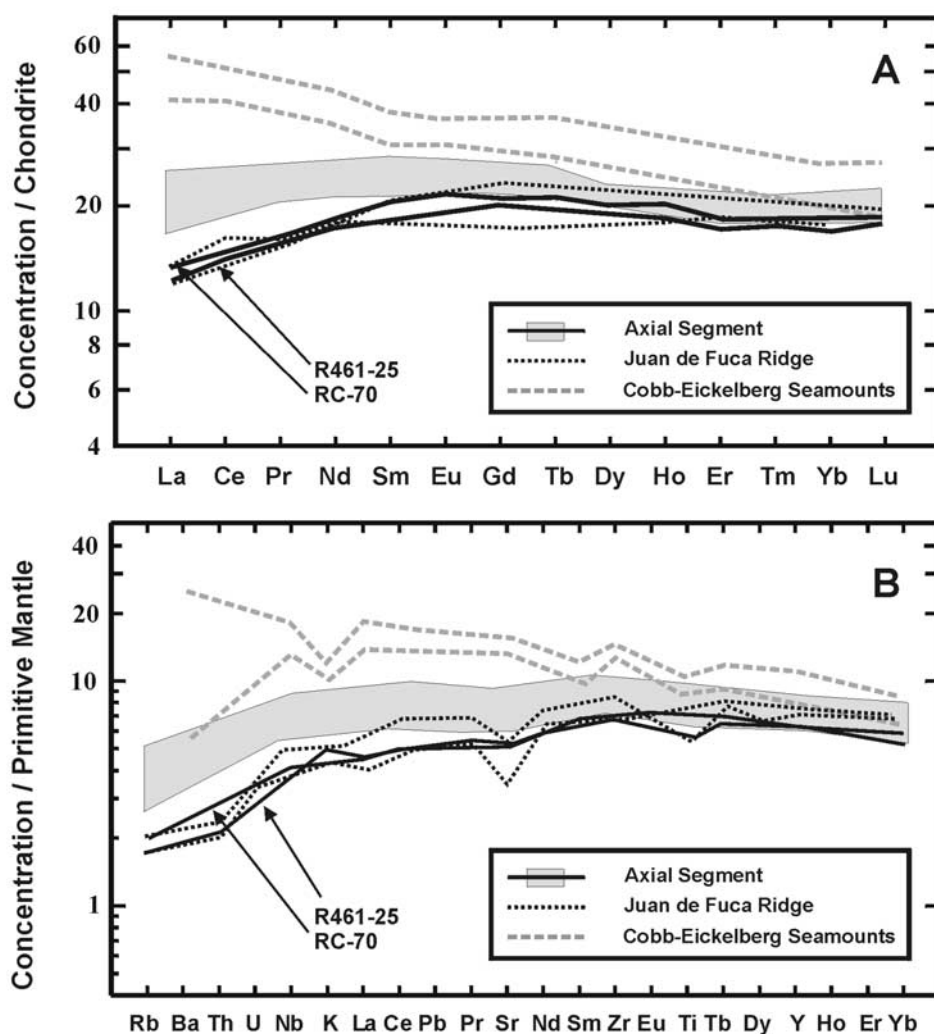


**Figure 7.** Most Axial Segment basalts have relatively flat ( $Ce_N/Yb_N \sim 1$ ) rare earth element patterns (shaded area represents 25 Axial Segment compositions) that are distinctly enriched in light REE relative to the typical depleted MORB patterns exhibited by basalts from the neighboring JdFR Segments. (a) MORB-like REE patterns and (b) multielement patterns and depleted trace element compositions exhibited by a few basalts, such as R461-25 and RC-70 (arrows), suggest that they represent indigenous MORB that is occasionally erupted on the Axial Segment. Cobb-Eickelberg seamount data are from *Desonie and Duncan [1990]*. Chondrite and mantle normalizing values are from *McDonough and Sun [1995]* and *Sun and McDonough [1989]*, respectively.

in which the voluminous seamount group lavas result from a shorter melting column as well as a lower melt fraction than ridge group lavas.

[30] A second melting model involves repeated melting episodes, resulting in progressive depletions in incompatible elements in a region of mantle over time. In this situation the Cobb plume rises vertically and generates melts by adiabatic decompression to feed Axial Seamount, which results in a more depleted plume source. If this region of the plume subsequently flows radially outward after encountering the base of the lithosphere as many models suggest [e.g., *Sleep*, 1996], it will then flow subhorizontally beneath the rift zones and may undergo additional episodes of melting because of ridge extension and decompression. These repeated melting events in the laterally migrating mantle would result in progressive depletions and potentially in the declining gradients observed in incompatible trace elements along the rift zones. This scenario should also result in depletions in incompatible major elements. However,  $\text{TiO}_2$  and  $\text{Na}_2\text{O}$ , which are both more incompatible than several trace elements that are depleted in the ridge group (e.g., Y and Yb), are instead increasingly enriched with increasing distance from Axial Seamount (Figure 4). Instead of melting, the concentrations of these elements follow calculated liquid lines of descent and appear to be largely controlled by fractional crystallization (Figure 3). Therefore this melting model also does not appear to be responsible for the geochemical observations.

#### 4.3. Mixing Effects

[31] The similarity of radiogenic isotopes in JdFR, Cobb hot spot, and Axial Segment basalts renders the identification of differences in magmatic sources more difficult than in most ridge-hot spot studies. However, the physical superposition of the hot spot and ridge magmatic systems and the observation of Axial Segment trace element compositions that are intermediate between those of the Cobb-Eickelberg seamounts and JdFR suggest that mixing of these two end-members has taken place to produce hybrid Axial Segment lavas. The morphological influence of hot spot magmas on the Axial Segment has been clearly shown, and the occurrence of a few basalts with more depleted trace element compositions and characteristic NMORB-like REE patterns (Figures 6 and 7) suggests that indigenous JdFR MORB magma is available for mixing with hot spot magmas. This more depleted lava type was also noted by *Rhodes et al.* [1990], who suggested that these samples represent MORB that had avoided mixing in the Axial Seamount magmatic system. That these MORB-like basalts can occasionally erupt at Axial Seamount without interacting with the more common, more enriched magmas suggests that the magma body underlying the volcano may be ephemeral or may shrink at times, allowing the MORB melts to erupt.

[32] The results of mixing calculations [after *Langmuir et al.*, 1978] between enriched Cobb-Eickelberg and depleted JdFR basalt compositions are shown in Figure 6 and indicate that these are viable mixing end-members for producing the Axial Segment suite. Furthermore, these results predict the proportions of the two components that are required to produce the observed hybrid lavas, suggesting that they contain between  $\sim 0$  and 60% of the Cobb hot

spot component, with most containing between 20 and 40% and dominated by the MORB end-member. This result is in general agreement with geophysical studies that suggest an  $\sim 30\%$  increase in crustal production at Axial Seamount due to the presence of the hot spot [*Hooft and Detrick*, 1995].

[33] The most enriched basalts recovered from the Axial Segment, those from Axial Seamount that are modeled to contain the highest proportion of the Cobb hot spot component, are nonetheless more depleted than any recovered elsewhere on the Cobb-Eickelberg chain. This is possibly the result of entrainment of MORB mantle in the plume (Figure 8) and is an effect that has increased in the Cobb hot spot over at least the past 8 m.y. In the hot spot chain, alkali and light rare earth element enrichments decrease with decreasing seamount age [*Desonie and Duncan*, 1990], suggesting an increasing influence of the depleted component as the ridge approached the hot spot. This observation indicates that the Cobb-Eickelberg “end-members” used in the mixing calculations should not be considered to be a true representation of the uncontaminated Cobb hot spot and that the mixing proportions of the MORB end-member in Axial Segment basalts are probably higher than the calculations suggest. Additional geochemical data from the central and western portions of the hot spot chain will be required to elucidate the uncontaminated geochemical signature of the hot spot.

[34] For mixing to explain the trace element gradients observed on the Axial Segment the proportion of the MORB component must progressively increase at the expense of the more enriched hot spot component along the rift zones with distance from Axial Seamount. A scenario in which the depth to the MORB source gradually decreases as the plume flattens and thins below the base of the lithosphere is shown in Figure 8. In this conceptual model, as the distance from Axial Seamount increases, the proportion of MORB melts in melting columns gradually increases as the contribution from hot spot melt decreases. Mixing in this manner would account for the negative incompatible trace element gradients but would have a limited effect on major element concentrations since the plume and MORB have similar concentrations of these elements. Major element gradients are largely controlled by postmixing fractional crystallization as explained above.

#### 5. Conclusions

[35] Analyses of basalts collected along the Axial Segment of the Juan de Fuca Ridge have revealed geochemical gradients in major and trace elements. The maxima or minima of these gradients are at Axial Seamount, the locus of the Cobb hot spot. The gradients are inversely correlated, with progressively more evolved and incompatible element-depleted lavas erupted with increasing distance from the Cobb hot spot. Basalts from the Axial Segment have alkali and incompatible trace element concentrations that fall largely in intermediate ranges between values for the Cobb hot spot and JdFR basalts. These observations can be explained by mixing between MORB and hot spot magmas, with the proportion of MORB in the hybrid magma increasing with distance from the hot spot, coupled with the increasing efficiency of fractional crystallization due to

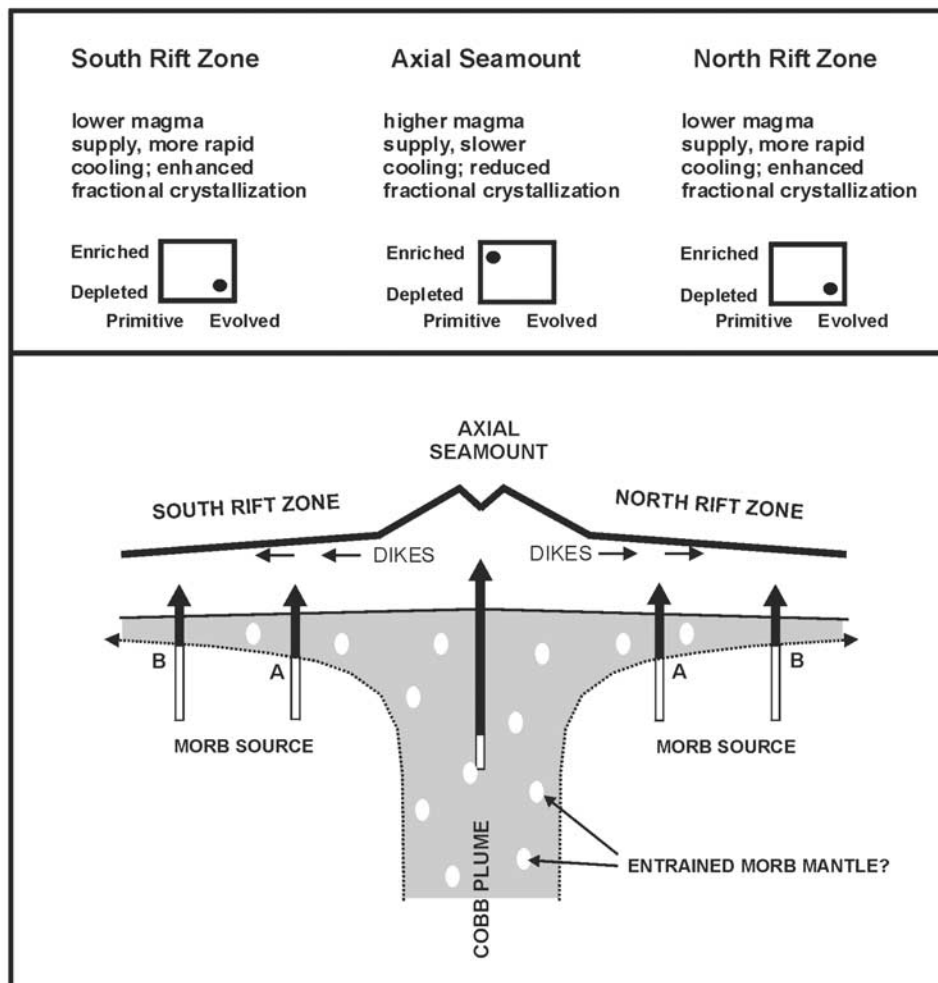


**Figure 8.** Conceptual model to explain the geochemical gradients observed on the Axial Segment is shown. Magmas at Axial Seamount likely reside in larger magma bodies in hotter crust, which would inhibit fractional crystallization. With increasing distance from Axial Seamount along the rift zones, smaller magma chambers may be emplaced in cooler crust, leading to more efficient fractional crystallization and more evolved lavas. Incompatible element gradients may result from a progressively flattening and thinning Cobb hot spot plume beneath the rift zones (from arrow labeled A to arrow labeled B), thus decreasing the depth to the MORB source and leading to an increasing relative contribution of MORB magmas (open part of arrows) mixing with hot spot magmas (solid part of arrows) and progressively more depleted lavas along the rift zones. Axial Seamount lavas also contain a significant proportion of the MORB mixing component, possibly because of entrainment of MORB mantle material by the Cobb hot spot. Dikes in the crust laterally disperse magmas along the rift zones prior to eruption.

a decrease in magma supply and faster cooling rates. A few basalts have distinct, depleted compositions that are geochemically similar to MORB found elsewhere on the JdFR, including more depleted trace element concentrations and MORB-like REE patterns. These basalts presumably represent indigenous Juan de Fuca Ridge MORB that have avoided mixing with Cobb hot spot magmas.

#### Appendix A: Analytical Methods

[36] Major element and some minor element analyses ( $\text{SiO}_2$ ,  $\text{Al}_2\text{O}_3$ ,  $\text{TiO}_2$ ,  $\text{FeO}$ ,  $\text{MnO}$ ,  $\text{MgO}$ ,  $\text{CaO}$ ,  $\text{K}_2\text{O}$ ,  $\text{Na}_2\text{O}$ , and  $\text{P}_2\text{O}_5$ ) of natural glasses were performed by electron microprobe at the U.S. Geological Survey in Denver,

Colorado, and at Florida International University in Miami, Florida. The freshest glass chips (100–500 mg) were handpicked under a microscope to choose those that were most free of alteration, and these were ensonicated for 3 min in a dilute hydrochloric acid and hydrogen peroxide solution. The microprobes typically analyzed a line of 10- $\mu\text{m}$  target spots on the glass chips. Major element values are normalized to internal standards (internal standards JDF and 2392-9) and are averages of 6–10 spots on each sample, and rare spurious compositions caused by microphenocrysts were excluded.

[37] Trace element analyses were performed on 30-mm-diameter pressed powder pellets with the X-ray fluorescence spectrometer at the Department of Geological Sciences at

the University of Florida. Phenocryst-free glass chips for the pellets were coarsely crushed in a jaw crusher or cross-beater mill, ensonicated in dilute hydrochloric acid and hydrogen peroxide solution, and powdered in an agate ball mill for three 12-min intervals to a fine powder. Powders were mixed with methylene chloride binder solution (0.5 mL/g of sample) and pressed for 5 min at  $2 \times 10^8$  Pa (30,000 psi). Spectrometer matrix effects were corrected by monitoring the Rh Compton peak, and instrumental drift, accuracy, and precision were monitored using basalt standards (internal standard ENDV and BHVO) with each spectrometer run of 5–15 samples. Selected samples were also analyzed for trace element composition, including rare earths, using inductively coupled plasma–mass spectrometry (ICP-MS) at the Geological Survey of Canada.

[38] Radiogenic isotopic analyses were performed at the Department of Geological Sciences at the University of Florida. About 0.1 g of rock powders were dissolved by heating in sealed Teflon vials for several days at 100°C in an HF-HNO<sub>3</sub> mixture. The vials were then opened and evaporated in a laminar flow hood in a clean lab class 1000 environment. For Sr and Nd isotopic analyses the dry residues were converted to chlorides with HCl, and Sr and Nd were separated using standard chromatographic methods [Richard *et al.*, 1976]. Lead was separated and purified with cation exchange columns in HBr medium, following the procedure of Manhes *et al.* [1978].

[39] Sr isotope measurements were collected using a Micromass Sector 54 thermal ionization mass spectrometer equipped with seven Faraday collectors and one Daly collector. Sr samples were loaded on oxidized W single filaments and run in dynamic collector mode. Data were acquired at a beam intensity of 1.5 V total Sr, with corrections for instrumental discrimination made assuming  $^{86}\text{Sr}/^{88}\text{Sr} = 0.1194$ . Errors in measured  $^{87}\text{Sr}/^{86}\text{Sr}$  are better than  $\pm 0.00002$  ( $2\sigma$ ) on the basis of long-term reproducibility of NBS 987 ( $^{87}\text{Sr}/^{86}\text{Sr} = 0.71024$ ).

[40] Nd isotopic analyses were performed on a Nu Plasma multiple collector magnetic sector inductively coupled mass spectrometer (MC-ICP-MS). Samples and standard solutions were aspirated into the plasma source via a Micromist nebulizer with GE spray chamber (wet plasma mode). The instrument settings were carefully tuned to maximize the signal intensities on a daily basis. Preamplifier gain calibration was performed before each analytical session. Nd isotope measurements were conducted for 60 ratios in static mode acquiring simultaneously  $^{142}\text{Nd}$  on low-2,  $^{143}\text{Nd}$  on low-1,  $^{144}\text{Nd}$  on axial,  $^{145}\text{Nd}$  on high-1,  $^{146}\text{Nd}$  on high-2,  $^{147}\text{Sm}$  on high-3,  $^{148}\text{Nd}$  on high-4, and  $^{150}\text{Nd}$  on high-5 Faraday detectors. The measured  $^{144}\text{Nd}$ ,  $^{148}\text{Nd}$ , and  $^{150}\text{Nd}$  beams were corrected for isobaric interference from Sm using  $^{147}\text{Sm}/^{144}\text{Sm} = 4.88$ ,  $^{147}\text{Sm}/^{148}\text{Sm} = 1.33$ , and  $^{147}\text{Sm}/^{150}\text{Sm} = 2.03$ . All measured ratios were normalized to  $^{146}\text{Nd}/^{144}\text{Nd} = 0.7219$  using an exponential law for mass bias correction. The mean value of  $^{143}\text{Nd}/^{144}\text{Nd}$  for the Ames Nd in-house standard based on 23 repeat analyses during the samples analyses was 0.512140 ( $2\sigma = 0.000012$ ). Three repeated analyses of the JNdi-1 and La Jolla Nd standards during the same time interval produced mean values of 0.512106 ( $2\sigma = 0.000013$ ) and 0.511856 ( $2\sigma = 0.000013$ ), respectively. Three samples of U.S. Geological Survey SRM BCR-1

(Columbia River basalt) were prepared and analyzed for Nd isotopes together with the samples in order to further evaluate the analytical protocol. The mean value of  $^{143}\text{Nd}/^{144}\text{Nd}$  for the analyses of BCR-1 was 0.512645 ( $2\sigma = 0.000011$ ), which is indistinguishable from the published thermal ionization mass spectrometer value of 0.51264 [Gladney *et al.*, 1990].

[41] Pb isotopic analyses were also conducted on the Nu Plasma MC-ICP-MS using the Tl normalization technique [e.g., Rehkämper and Halliday, 1998]. Sample and standard solutions were aspirated into the plasma source in wet plasma mode. All analyses reported in this paper were conducted in static mode acquiring simultaneously  $^{202}\text{Hg}$  on low-1,  $^{203}\text{Tl}$  on low-2,  $^{204}\text{Pb}$  on axial,  $^{205}\text{Tl}$  on high-1,  $^{206}\text{Pb}$  on high-2,  $^{207}\text{Pb}$  on high-3, and  $^{208}\text{Pb}$  on high-4 Faraday detectors. Forty-two analyses of NBS 981 conducted with the sample analyses in the period between April and June 2003 gave the following results:  $^{206}\text{Pb}/^{204}\text{Pb} = 16.9369$  ( $\pm 0.0039$  2 SE),  $^{207}\text{Pb}/^{204}\text{Pb} = 15.4904$  ( $\pm 0.0034$  2 SE), and  $^{208}\text{Pb}/^{204}\text{Pb} = 36.6949$  ( $\pm 0.0087$  2 SE). All standard and sample Pb data were normalized with  $^{205}\text{Tl}/^{203}\text{Tl} = 2.38750$ . For more details, see Kamenov *et al.* [2004].

[42] Volatile (H<sub>2</sub>O, CO<sub>2</sub>, and S) and halogen (F and Cl) concentrations were measured using the Cameca ion mass spectrometer 6f ion probe at the Department of Terrestrial Magnetism, Carnegie Institution of Washington, Washington, D. C. [Hauri *et al.*, 2002]. Hand-picked, fresh, alteration-, crack-, and fracture-free, and aphyric MORB quenched glass shards were mounted in epoxy in holes drilled in a 25-mm round aluminum disc. Polished and cleaned discs (P. J. le Roux *et al.*, Volatile (H<sub>2</sub>O, CO<sub>2</sub>, S) and halogen (F, Cl) compositions of northern EPR MORB (8–10°N and 12–14°N): Evidence of variable magma contamination, manuscript in preparation, 2004) were dried in an oven at  $\sim 70^\circ\text{C}$  for a few hours before being gold coated. Three shards from each sample were analyzed to assess compositional homogeneity. The routine detection limits for the volatiles and halogens were <10–30 ppm H<sub>2</sub>O, <3 ppm CO<sub>2</sub>, and <1 ppm F, S, and Cl, significantly below the concentrations in the samples, and the average accuracy was better than  $\sim 10\%$  [Hauri *et al.*, 2002].

[43] **Acknowledgments.** The authors wish to thank Randy Keller, David Clague, and Associate Editor Emily Klein for their very helpful reviews. We also thank the crews of the R/V *Ronald Brown* and R/V *Thomas Thompson* for transporting us to a very remote field area and for rock coring assistance, and we thank the *ROPOS* team for helping us to retrieve samples from the ocean floor. We thank Claire Chadwick for her help with sample preparation. The NOAA VENTS Program and West Coast and Polar Regions Undersea Research Center provided support for ship time and *ROPOS* dives at the NeMO seafloor observatory. The field and laboratory research was also supported by the National Science Foundation (OCE-9530299 to M.R.P.). We also thank Peter Belanger and staff, Analytical Chemistry Section, Mineral Resources Division, Geological Survey of Canada. J.C. acknowledges the McLaughlin Dissertation Fellowship, the Thompson Fellowship, and a College of Liberal Arts and Sciences Research Fellowship, which supported portions of his education and research at the University of Florida. PMEL contribution 2733. I.R. published with permission of the Director, U.S. Geological Survey.

## References

- Appelgate, T. B., Jr. (1990), Volcanic and structural morphology of the south flank of Axial Volcano, Juan de Fuca Ridge: Results from a Sea MARC I side scan survey, *J. Geophys. Res.*, *95*, 12,765–12,783.
- Chadwick, J. (2002), Magmatic and tectonic effects of the interaction of the Juan de Fuca mid-ocean ridge with the Cobb hotspot, Ph.D. thesis, 135 pp., Dep. of Geol. Sci., Univ. of Fla., Gainesville.

- Chadwick, W. W., Jr., R. W. Embley, and S. Merle (2002), Emplacement processes of two 1998 lava flows with contrasting morphology, inferred from high-resolution bathymetry and bottom observations at Axial Seamount, Juan de Fuca Ridge, *Eos Trans. AGU*, 83, Ocean Sci. Meet. Suppl., Abstract OS41L-02.
- Christie, D. M., and J. M. Sinton (1981), Evolution of abyssal lavas along propagating segments of the Galapagos spreading center, *Earth Planet. Sci. Lett.*, 56, 321–335.
- Church, S. E., and M. Tatsumoto (1975), Lead isotope relations in oceanic ridge basalts from the Juan de Fuca–Gorda Ridge area, Pacific Ocean, N.E., *Contrib. Mineral. Petrol.*, 53, 253–279.
- Danyushevsky, L. (2001), The effect of small amounts of H<sub>2</sub>O on crystallization of mid-ocean ridge and backarc basin magmas, *J. Volcanol. Geotherm. Res.*, 110, 265–280.
- Delaney, J. R., H. P. Johnson, and J. L. Karsten (1981), The Juan de Fuca Ridge-hotspot-propagating rift system: New tectonic, geochemical, and magnetic data, *J. Geophys. Res.*, 86, 11,747–11,750.
- Desonie, D. L., and R. A. Duncan (1986), Spreading ridge and hotspot contributions to seamounts near the Juan de Fuca Ridge (abstract), *Eos Trans. AGU*, 67, 1231.
- Desonie, D. L., and R. A. Duncan (1990), The Cobb-Eickelberg seamount chain: Hotspot volcanism with mid-ocean ridge basalt affinity, *J. Geophys. Res.*, 95, 12,697–12,711.
- Dziak, R. P., and C. G. Fox (1998), Hydroacoustic detection of submarine volcanic activity at Axial Volcano, Juan de Fuca Ridge, January, 1998 (abstract), *Eos Trans. AGU*, 79, Fall Meet. Suppl., F922.
- Dziak, R. P., and C. G. Fox (1999), The January, 1998 earthquake swarm at Axial Volcano, Juan de Fuca Ridge: Hydroacoustic evidence for seafloor volcanic activity, *Geophys. Res. Lett.*, 26, 3425–3428.
- Eaby, J., D. A. Clague, and J. R. Delaney (1984), Sr isotopic variations along the Juan de Fuca Ridge, *J. Geophys. Res.*, 89, 7883–7890.
- Elliot, T. R., C. J. Hawkesworth, and K. Gronvold (1991), Dynamic melting of the Iceland plume, *Nature*, 351, 201–206.
- Embley, R. W., K. M. Murphy, and C. G. Fox (1990), High-resolution studies of the summit of Axial Volcano, *J. Geophys. Res.*, 95, 12,785–12,812.
- Embley, R. W., W. W. Chadwick, D. A. Clague, and D. Stakes (1999), 1998 eruption of Axial Volcano: Multibeam anomalies and seafloor observations, *Geophys. Res. Lett.*, 26, 3425–3428.
- Embley, R. W., W. W. Chadwick, M. R. Perfit, M. C. Smith, and J. R. Delaney (2000), Recent eruptions on the CoAxial Segment of the Juan de Fuca Ridge: Implications for mid-ocean ridge accretion processes, *J. Geophys. Res.*, 105, 16,501–16,525.
- Fox, C. G., W. W. Chadwick, and R. W. Embley (2001), Direct observations of a submarine volcanic eruption from a sea-floor instrument caught in a lava flow, *Nature*, 412, 727–729.
- Gladney, E. S., E. A. Jones, E. J. Nickell, and I. Roelandts (1990), Compilation of elemental concentration data for USGS basalt BCR-1, *Geostand. News.*, 14, 209–359.
- Hardarson, B. S., J. G. Fitton, R. M. Ellam, and M. S. Pringle (1997), Rift relocation: A geochemical and geochronological investigation of a paleo-rift in northwest Iceland, *Earth Planet. Sci. Lett.*, 153, 181–196.
- Hart, S. R., J. G. Schilling, and J. L. Powell (1973), Basalts from Iceland and along the Reykjanes Ridge: Sr isotope geochemistry, *Nature*, 246, 104–107.
- Hart, S. R., E. H. Hauri, L. A. Oschmann, and J. A. Whitehead (1992), Mantle plumes and entrainment: Isotopic evidence, *Science*, 256, 517–520.
- Hauri, E. H., J. Wand, J. E. Dixon, P. L. King, C. Mandeville, and S. Newman (2002), SIMS analysis of volatiles in silicate glasses 1. Calibration, matrix effects and comparisons with FTIR, *Chem. Geol.*, 183, 99–114.
- Hegner, E., and M. Tatsumoto (1987), Pb, Sr, and Nd isotopes in basalts and sulfides from the Juan de Fuca Ridge, *J. Geophys. Res.*, 92, 11,380–11,386.
- Hegner, E., and M. Tatsumoto (1989), Pb, Sr, and Nd isotopes in seamount basalts from the Juan de Fuca Ridge and Kodiak-Bowie seamount chain, northeast Pacific, *J. Geophys. Res.*, 94, 17,839–17,846.
- Hooft, E. E., and R. S. Detrick (1995), Relationship between axial morphology, crustal thickness, and mantle temperature along the Juan de Fuca and Gorda Ridges, *J. Geophys. Res.*, 100, 22,499–22,508.
- Johnson, H. P., and R. W. Embley (1990), Axial Seamount: An active ridge axis volcano on the central Juan de Fuca Ridge, *J. Geophys. Res.*, 105, 12,689–12,696.
- Johnson, H. P., and M. L. Holmes (1989), Evolution in plate tectonics; the Juan de Fuca Ridge, in *The Geology of North America*, vol. N, *The Eastern Pacific Ocean and Hawaii*, edited by E. L. Winterer, D. M. Hussong, and R. W. Decker, pp. 73–91, Geol. Soc. of Am., Boulder Colo.
- Kamenov, G. D., P. A. Mueller, and M. R. Perfit (2004), Optimization of mixed Pb-Tl solutions for high precision isotopic analyses by MC-ICP-MS, *J. Anal. At. Spectrom.*, 19(9), 1262–1267, doi:10.1039/b403222e.
- Karsten, J. L., and J. R. Delaney (1989), Hot spot-ridge crest convergence in the northeast Pacific, *J. Geophys. Res.*, 94, 700–712.
- Karsten, J. L., S. R. Hammond, E. E. Davis, and R. G. Currie (1986), Detailed geomorphology and neotectonics of the Endeavor Segment, Juan de Fuca Ridge: New results from Seabeam swath mapping, *Geol. Soc. Am. Bull.*, 97, 213–221.
- Karsten, J. L., J. R. Delaney, J. M. Rhodes, and R. A. Liias (1990), Spatial and temporal evolution of magmatic systems beneath the Endeavor Segment, Juan de Fuca Ridge: Tectonic and petrologic constraints, *J. Geophys. Res.*, 95, 19,235–19,256.
- Keller, R. A., M. R. Fisk, R. A. Duncan, and W. M. White (1997), 16 m.y. of hotspot and nonhotspot volcanism on the Patton-Murray seamount platform, Gulf of Alaska, *Geology*, 25(6), 511–514.
- Keller, R. A., M. Fisk, R. Duncan, M. Rowe, C. Russo, and R. Dziak (2003), Cobb hotspot volcanism prior to 7 million years ago, *Eos Trans. AGU*, 84, Fall Meet. Suppl., Abstract V32A-1002.
- Klein, E. M., and C. H. Langmuir (1987), Global correlations of ocean ridge basalt chemistry with axial depth and crustal thickness, *J. Geophys. Res.*, 92, 8089–8115.
- Langmuir, C. H., and J. F. Bender (1984), The geochemistry of oceanic basalts in the vicinity of transform faults: Observations and implications, *Earth Planet. Sci. Lett.*, 69, 107–127.
- Langmuir, C. H., R. D. Vocke, G. N. Hanson, and S. R. Hart (1978), A general mixing equation with applications to Icelandic basalts, *Earth Planet. Sci. Lett.*, 37, 380–392.
- Liias, R. A. (1986), Geochemistry and petrogenesis of basalts erupted along the Juan de Fuca Ridge, Ph.D. thesis, Univ. of Mass., Amherst.
- Manhes, G., J. F. Minster, and C. J. Allegre (1978), Uranium-thorium-lead and rubidium-strontium study of the saint Severing amphoterite; consequences for early solar system chronology, *Earth Planet. Sci. Lett.*, 39, 14–24.
- McDonough, W. F., and S.-S. Sun (1995), The composition of the Earth, *Chem. Geol.*, 120, 223–253.
- Murton, J. B., R. N. Taylor, and M. F. Thirlwall (2002), Plume-ridge interaction: A geochemical perspective from the Reykjanes Ridge, *J. Petrol.*, 43(11), 1987–2012.
- Oskarsson, N., S. Steinthorsson, and G. E. Sigvaldason (1985), Iceland geochemical anomaly: Origin, volcanotectonics, chemical fractionation and isotope evolution of the crust, *J. Geophys. Res.*, 90, 10,011–10,025.
- Perfit, M. R., A. L. Heatherington, S. Hughes, I. R. Jonasson, and J. M. Franklin (1988), Geochemistry of basalts from Axial Volcano: An example of a well-mixed magma chamber (abstract), *Eos Trans. AGU*, 69, 1467.
- Perfit, M. R., D. A. Stakes, W. I. Ridley, T. Ramirez, J. Kela, and S. Kulp (2001), Evaluation of the split-ridge hypothesis and generation of oceanic crust along the Cleft Segment of the southern Juan de Fuca Ridge (JdFR), *Eos Trans. AGU*, 82(47), Fall Meet. Suppl., Abstract F1278.
- Rehkämper, M., and A. N. Halliday (1998), Accuracy and long-term reproducibility of lead isotopic measurements by multiple-collector inductively coupled plasma mass spectrometry using an external method for correction of mass discrimination, *Int. J. Mass Spectrom.*, 181, 123–133.
- Rhodes, J. M. (1988), Geochemistry of the 1984 Mauna Loa eruption: Implications for magma storage and supply, *J. Geophys. Res.*, 93, 4453–4466.
- Rhodes, J. M., C. Morgan, and R. A. Liias (1990), Geochemistry of Axial Seamount lavas: Magmatic relationship between the Cobb hotspot and the Juan de Fuca Ridge, *J. Geophys. Res.*, 95, 12,713–12,733.
- Richard, P., N. Shimazu, and C. J. Allegre (1976), <sup>143</sup>Nd/<sup>144</sup>Nd, a natural tracer: An application to oceanic basalt, *Earth Planet. Sci. Lett.*, 31, 269–278.
- Schilling, J. G. (1973), Iceland mantle plume: Geochemical evidence along Reykjanes Ridge, *Nature*, 242, 565–571.
- Schilling, J. G., R. N. Anderson, and P. R. Vogt (1976), Rare earth and FeTi variations along the Galapagos spreading center and their relation to the Galapagos plume, *Nature*, 242, 108–113.
- Schilling, J.-G., D. Fontignie, J. Blichert-Toft, R. Kingsley, and U. Tomza (2003), Pb-Hf-Nd-Sr isotope variations along the Galapagos Spreading Center (101°–83°W): Constraints on the dispersal of the Galapagos mantle plume, *Geochim. Geophys. Geosyst.*, 4(10), 8512, doi:10.1029/2002GC000495.
- Sleep, N. H. (1996), Lateral flow of hot plume material ponded at sublithospheric depths, *J. Geophys. Res.*, 101, 28,065–28,083.
- Smith, M. (1999), Geochemistry of eastern Pacific MORB: Implications for MORB petrogenesis and the nature of crustal accretion within the

- neovolcanic zone of two recently active ridge segments, Ph.D. thesis, 164 pp., Dep. of Geol. Sci., Univ. of Fla., Gainesville.
- Smith, M. C., M. R. Perfit, and I. R. Jonasson (1994), Petrology and geochemistry of basalts from the southern Juan de Fuca Ridge: Controls on the spatial and temporal evolution of mid-ocean ridge basalt, *J. Geophys. Res.*, *99*, 4787–4812.
- Smoot, N. C. (1985), Observations of Gulf of Alaska seamount chains by multibeam sonar, *Tectonophysics*, *115*, 235–246.
- Sun, S.-S., and W. F. McDonough (1989), Chemical and isotopic systematics of oceanic basalts: Implications for mantle composition and process, in *Magmatism in the Ocean Basins*, edited by A. D. Saunders and M. J. Norry, *Geol. Soc. Spec. Publ.*, *42*, 313–345.
- Talwani, M., W. W. Windisch, and M. G. Langseth (1971), The Reykjanes Ridge crest: A detailed geophysical study, *J. Geophys. Res.*, *76*, 473–577.
- Van Wagoner, N. A., and M. I. Leybourne (1991), Evidence for mixing and a heterogeneous mantle on the West Valley Segment of the Juan de Fuca Ridge, *J. Geophys. Res.*, *96*, 16,295–16,318.
- Vine, F. J., and J. T. Wilson (1965), Magnetic anomalies over a young oceanic ridge off Vancouver Island, *Science*, *150*, 485–489.
- West, M., W. Menke, M. Tolstoy, S. Webb, and R. Sohn (2001), Magma storage beneath Axial volcano on the Juan de Fuca mid-ocean ridge, *Nature*, *25*, 833–837.
- 
- W. Chadwick and R. Embley, Hatfield Marine Science Center, NOAA/PMEL, Oregon State University, 2115 SE Oregon State University Drive, Newport, OR 97365-5258, USA.
- J. Chadwick, Department of Geosciences, Idaho State University, Pocatello, ID 83209, USA. (chadjohn@isu.edu)
- I. Jonasson, Natural Resources Canada, Geological Survey of Canada, 601 Booth Street, Room 752, Ottawa, Ontario, Canada K1A 0E8.
- G. Kamenov, M. Perfit, and M. Smith, Department of Geological Sciences, University of Florida, 241 Williamson Hall, Gainesville, FL 32611-2120, USA.
- P. le Roux, Department of Terrestrial Magnetism, Carnegie Institution of Washington, 5241 Broad Branch Road, N. W., Washington, DC 20015, USA.
- I. Ridley, U.S. Geological Survey, Denver Federal Center, MS 973, Denver, CO 80225, USA.